Understanding ENSO Regime Behavior upon an Increase in the Warm-Pool Temperature Using a Simple ENSO Model

BAEK-MIN KIM

Korea Polar Research Institute, Incheon, Korea

SOON-IL AN

Department of Atmospheric Sciences, Yonsei University, Seoul, Korea

(Manuscript received 26 January 2010, in final form 22 June 2010)

ABSTRACT

The regime behavior of the low-order El Niño–Southern Oscillation (ENSO) model, according to an increase in the radiative–convective equilibrium sea surface temperature (SST; T_r), is studied to provide a possible explanation for the observed increase in ENSO irregularity characterized by decadal modulation. During recent decades, a clear increasing trend of the warm-pool SST has been observed. In this study, the increase in the warm-pool maximum SST is interpreted as an increase in T_r following previous studies. A bifurcation analysis with T_r as a control parameter is conducted to reveal that the degree of ENSO irregularity in the model is effectively controlled by the equilibrium states of the model. At a critical value of T_r, bifurcation analysis reveals that period-doubling bifurcation occurs and an amplitude-modulated ENSO emerges. At this point, a subcycle appears within the preexisting ENSO cycle, which initiates decadal modulation of ENSO. As T_r increases further, nested oscillations are successively generated, illustrating clear decadal modulation of ENSO. The qualitative regime changes revealed in this study are supported by the observation of regime shifts in the 1970s. With increasing T_r, the mean zonal SST gradient increases, and the model adjusts toward a ''La Niña–like'' mean state. Further constraint with shoaling of the mean thermocline depth and increasing stratification causes ENSO to exhibit stronger amplitude modulation. Furthermore, the timing of the period-doubling bifurcation advances with these two effects.

1. Introduction

How ENSO responds to global warming is a controversial issue and has attracted attention in recent literature. The characteristics of the El Niño–Southern Oscillation (ENSO) are known to depend on the tropical mean climate conditions, such as the mean thermocline depth, mean wind stress (An and Jin 2001; Fedorov and Philander 2000; Wang and An 2001), and the warm-pool temperature that defines the warmth of the tropical ocean (Sun 1997). Although early studies utilizing a fully coupled GCM suggested that global warming may result in little change to the amplitude of ENSO (Knutson and Manabe 1995), recent studies investigating future projections have demonstrated that slowly varying tropical mean climate conditions associated with global warming have profound impacts on ENSO characteristics (An et al. 2008; Collins 2005; Merryfield 2006; Timmermann et al. 1999). Nevertheless, inconsistencies still remain among the different models (Guilyardi 2006).

Whether the tropical Pacific response to future global warming is more El Niño–like or La Niña–like depends on a complex balance between various positive and negative feedback mechanisms that contribute to ENSO (Cane et al. 1997; Collins 2005; Karnauskas et al. 2009; Latif and Keenlyside 2008; Vecchi and Soden 2007). Clement et al. (1996) showed that the Zebiak–Cane model (Zebiak and Cane 1987) approaches a new equilibrium state of an increased zonal SST gradient when it is forced by uniform thermal radiative forcing. Observational reconstructions of SST during the twentieth century show a ''La Niña–like'' long-term trend (Cane et al. 1997; Karnauskas et al. 2009). Cane et al. (1997) explains that this observed La Niña–like trend is due to the large compensation of radiative heating by vigorous upwelling in the eastern Pacific

Corresponding author address: Soon-Il An, Dept. of Atmospheric Sciences, Yonsei University, 50 Yonsei-ro, Seodaemun-gu, Seoul 120-749, Korea.
E-mail: sian@yonsei.ac.kr

DOI: 10.1175/2010JCLI3635.1

bringing cold waters up through ocean dynamics. These observations seem to support Clement et al. (1996) and also seem to indicate that, in the tropical ocean, SST increases more in the west than in the east in response to global warming, thereby enhancing the temperature gradient along the equator—although the reliability of various SST reconstructions has been criticized (Vecchi et al. 2008). In contrast, the majority of coupled climate models predict an El Niño–like future climate (Cubasch et al. 2001; Meehl et al. 2007). A possible dynamical explanation for an El Niño–like response was also sought by examining changes in the off-equatorial precipitation pattern and the associated circulation changes (Kug et al. 2010). The discrepancies in the observations and projections seem to stem from the transient nature of tropical adjustment to global warming. An et al. (2008) pointed out that the behavior of ENSO can change depending on thermal stratification, which exhibits a delayed response to the degree of global warming progression. Considering the dependency of ENSO on the tropical mean climate, reaching a consensus on the future tropical mean state as global warming progresses is crucial to understanding the behavior of ENSO. Aside from the conflicting arguments about the tropical mean climate conditions associated with global warming, this study aims to understand the regime behavior of ENSO using a low-order ENSO model that favors the La Niña–like changes in a warming climate.

Sun (1997) suggested that El Niño can be interpreted as an eastward manifestation of warmth confined within the warm-pool region that is fundamentally controlled by the maximum SST (SST_{max}) in the warm-pool region. Because SST_{max} is highly correlated with the global mean surface temperature, it is a good indicator of global warming. He found that increasing SST_{max} also increases the magnitude and frequency of ENSO. This result was further supported by a detailed heat budget analysis and fully coupled GCM results (Sun 2003).

From a detailed analysis of the wavelet spectrum of the Niño-3 index, An and Wang (2000) concluded that ENSO was less frequent but had a higher magnitude after the mid-1970s. ENSO also exhibited irregular behavior, as compared to its behavior before the mid-1970s. A big El Niño event per decade, followed by small events, seems to be a repeating pattern. ENSO behavior after the mid-1970s is, therefore, characterized by intermittent oscillations and bursting. Timmermann et al. (2003) investigated the ''El Niño bursting'' and related it to regime shifts of nonlinear ENSO dynamics. They demonstrated that, in a low-order ENSO model, various regime behavior of ENSO—for example, regular-to-irregular ENSO changes as well as long-term changes in ENSO activity—are possible by controlling a parameter determining the strength of nonlinear advection. In reality, however, the strength of nonlinearity may not be externally maneuverable but is determined internally. In this study, we examine how ENSO responds to the observed increasing trend of SST_{max}, instead of directly controlling the degree of nonlinearity.

In section 2, we contrast the observed trends of SST_{max} and eastern Pacific SST during the twentieth century and discuss the implications of our findings. In section 3, we describe the model used in this study. The basic ENSO regime behavior revealed by bifurcation analysis is presented in section 4. In section 5, we examine the transient behavior of ENSO in response to increasing external forcing. Furthermore, we discuss the possible impact of changes in the mean thermocline depth on ENSO behavior.

2. Observed trend of maximum warm-pool temperature

We use the Met Office Hadley Centre's sea ice and SST dataset (HadISST1; Rayner et al. 2003) for the period from 1900 to 2006 to calculate SST_{max}. Although the analysis extends from 1856, we did not use the nineteenth-century data because of suspicions about the reconstructions (Lau et al. 1992). For each month of data, SST_{max} is simply the maximum value of SST in the region of 5°S–5°N. Without exception, SST_{max} is always found over the warm-pool region. Because both horizontal and vertical oceanic heat transport tends to cool the ocean surface, it is a reasonable approximation that SST_{max} is the temperature that the tropical ocean would attain in the absence of thermal advections in the observation (Sun 2003). Over the central region of the warm pool where SST_{max} is usually found, the net heat flux across the ocean surface is almost zero. Hence, we use SST_{max} as a physical approximation of the temperature of the radiative–convective equilibrium SST.

SST_{max} is shown as the moving average of 40-month windows and, as depicted in Fig. 1a (thick solid), shows an apparent linear trend with a rate of 0.5°C (century)$^{-1}$. It reaches about 30°C in the most recent decade. In contrast, examination of 40-month-averaged Niño-3 index in Fig. 1a (thin dashed) indicates that the trend over the eastern Pacific is much smaller than that over the western Pacific warm-pool region. This is consistent with Cane et al. (1997) who showed a nonincreasing mean eastern Pacific temperature when ENSO was removed.

The 11-month-averaged Niño-3 index obtained from HadISST1 from 1900 to 2006 is shown in Fig. 1b. As seen in the figure, El Niño peaks (particularly when measured by the Niño-3 index) before the mid-1970s are about 1°C higher than normal and never exceed 2°C. Bursting events, where the anomalies exceed 2°C, are observed only after the mid-1970s. Even without resorting

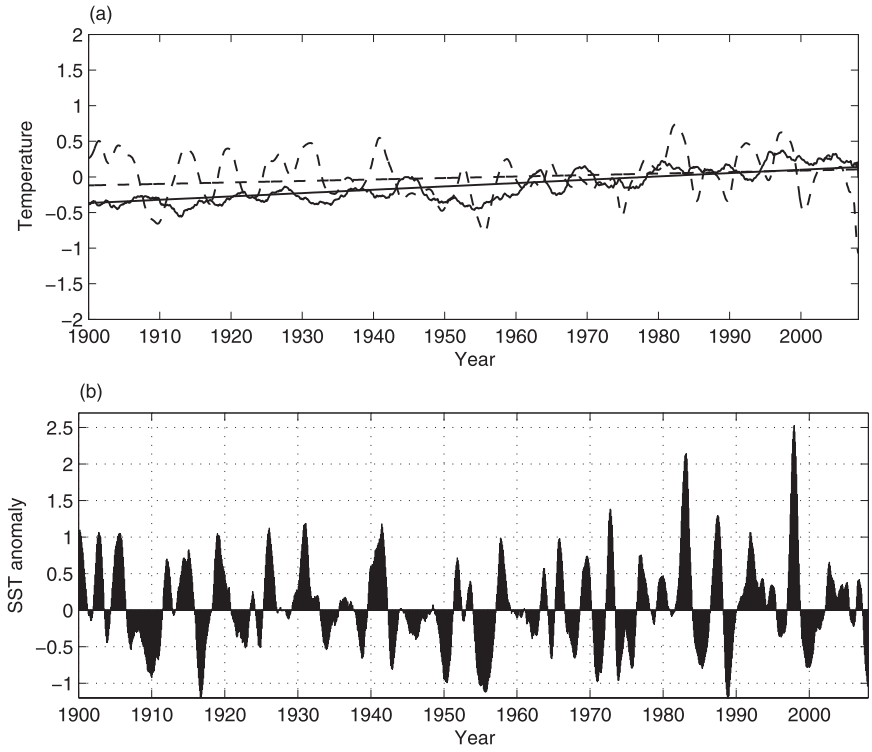

FIG. 1. (a) 40-month-averaged SST_{max} anomaly (thick solid) and SST anomaly over the Niño-3 region (thin dashed). The trend for each time series is represented by a straight line of the same color. (b) The Niño-3 index during the same period.

to sophisticated statistics, an ENSO regime change is recognizable.

3. Low-order ENSO model

The low-order ENSO model used in this study is a two-box representation of an intermediate tropical Pacific ocean–atmosphere coupled model (e.g., Zebiak and Cane 1987), which has been proved to capture the recharging/discharging oscillatory behavior of ENSO, including the period and the phase relationship between the variations of SST and the depth of the thermocline (Jin 1996; Sun 1997; Timmermann et al. 2003). The model comprises two boxes of the tropical western Pacific (135°E–155°W, 5°S–5°N) and the eastern Pacific (155°–85°W, 5°S–5°N) wherein variables are defined. SST and thermocline depth anomaly in the western box and SST in the eastern box are defined as prognostic variables denoted by T_1, h_1, and T_2, respectively. The thermocline depth anomaly is defined as the deviation from a predefined reference depth of the thermocline, which is denoted by H. Although essentially the same equation set has been presented several times in previous studies, we adopt the formulation of Timmermann et al. (2003) and repeat it here for clarity. The three model prognostic equations are as follows:

$$\frac{dT_1}{dt} = -\alpha(T_1 - T_r) - \varepsilon\beta\tau(T_2 - T_1), \tag{1}$$

$$\frac{dT_2}{dt} = -\alpha(T_2 - T_r) + \zeta\beta\tau(T_2 - T_{\text{sub}}), \quad \text{and} \tag{2}$$

$$\frac{dh_1}{dt} = r\left(-h_1 - \frac{bL\tau}{2}\right). \tag{3}$$

Here, T_r, the radiative–convective equilibrium SST, is the varying parameter in this study and can be approximately estimated by SST_{max}. The first terms on the right-hand side of Eqs. (1) and (2) represent bulk heat fluxes into the western and eastern boxes, respectively, with $1/\alpha$ as the thermal adjusting time scale toward T_r. The second terms in (1) and (2) represent the zonal thermal advection and the vertical thermal advection, respectively. Here, ε and ζ, nondimensional parameters, control the effective strength of thermal advection in each direction, respectively. Timmermann et al. (2003) varied ε and ζ for the bifurcation analysis to deal with the issue of ENSO regime behavior related to the intrinsic nonlinearity of the system. In this study, however, we simply fix these two nondimensional parameters as 0.13 and 1, respectively, which are typical tropical ocean values. The sensitivity of the results to these parameters is discussed in section 4.

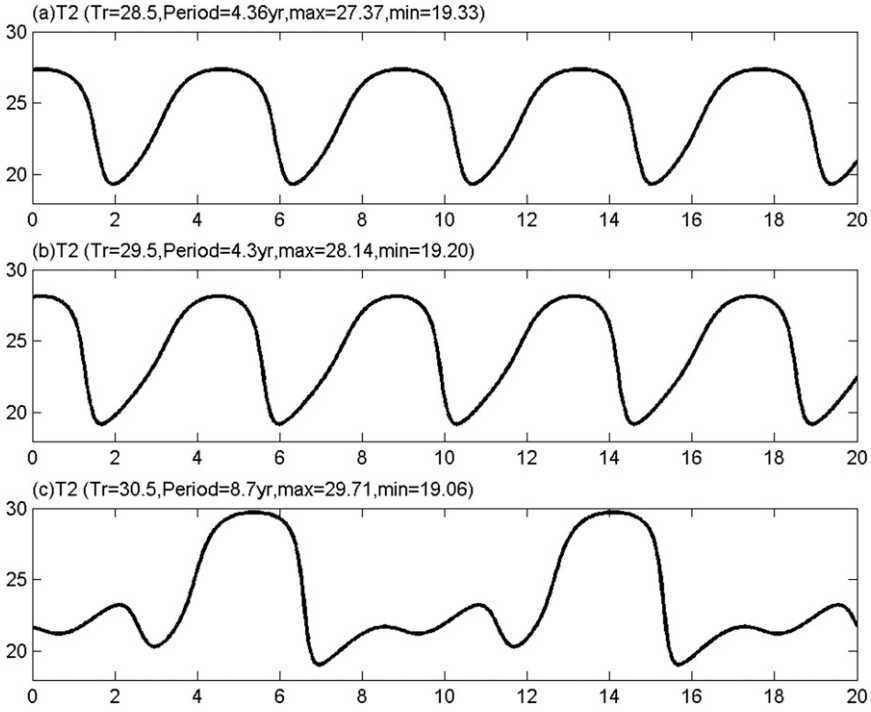

FIG. 2. Time series of T_2 depicted by time integration of the low-order ENSO model for (a) $T_r = 28.5$°C, (b) $T_r = 29.5$°C, and (c) $T_r = 30.5$°C after the initial transients have settled down. Among the three variables, T_2 was selected to represent the ENSO time series. The units of the time axis are years.

The anomalous zonal wind stress related to the Walker circulation τ is proportional to the zonal temperature gradient and expressed as $\tau = \mu(T_1 - T_2)/\beta$, where μ is a coupling coefficient, and β is the meridional gradient of planetary vorticity at the equator. Note that τ is an anomaly and does not contain components related to the Hadley circulation or other external sources. The eastern Pacific thermocline depth anomaly h_2 is diagnosed by $h_2 = h_1 + bL\tau$, where b is a measure of the efficiency of wind stress for deriving the west–east thermocline, and L is the basin width. The equation for the thermocline anomaly for the western box (h_1) is given in Eq. (3). It is governed by the basinwide adjustment process and zonally integrated Sverdrup meridional mass transport. The damping coefficient r is multiplied by $bL\tau/2$ to constrain the zonal mean thermocline depth at the equilibrium state to be the same as the reference depth. This implies $h_1 + h_2 = 0$ in the equilibrium state. Here, T_{sub} denotes the temperature of subsurface water being upwelled into the mixed layer of the eastern Pacific box. The subsurface temperature T_{sub} depends strongly on h_2 and is empirically parameterized as

$$T_{\text{sub}} = T_r - (T_r - T_c)/2[1 - \tanh(H + h_2 - z_0)/h^*], \quad (4)$$

where H is the reference depth of the mean thermocline for both h_1 and h_2, z_0 is the characteristic level at which upwelling occurs, T_c is the deep-ocean temperature below the thermocline, and h^* represents the degree of sharpness of the thermocline. Although this parameterization has been used in several previous studies (Jin 1996; Timmermann et al. 2003), no justification of the parameterization has been provided. Proper parameterization of T_{sub}, however, is important because its proper formulation is key to the thermocline feedback that is fundamental to ENSO. Therefore, in the appendix, we clarify how T_{sub} is formulated and how accurate it is compared to actual observations.

The qualitative dependency of ENSO on T_r in the low-order ENSO model is presented by showing a time series of ENSO at some typical values of T_r in Fig. 2. Time integration is conducted by applying a Runge–Kutta fourth-order scheme to Eqs. (1)–(3). The dynamical system exhibits a regular oscillation at $T_r = 28.5$°C, with a period of about 4.36 yr. A further increase in T_r slightly shortens the period of the oscillation. For $T_r = 29.5$°C, the period of the oscillation is about 4.3 yr. As T_r increases, the amplitude of ENSO becomes larger. The increase in frequency and amplitude of ENSO is consistent with the observed ENSO behavior as global warming progresses

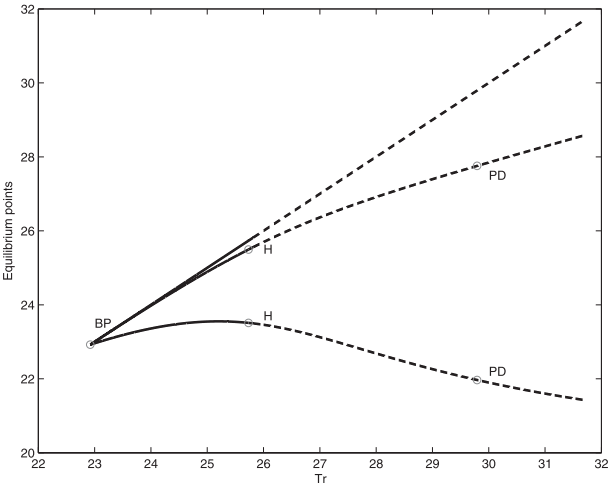

FIG. 3. Stability diagram showing the values of fixed points of the nonlinear ENSO model. The two equilibrium points, $(T_r, T_r, 0)$ and $(\overline{T_1}, \overline{T_2}, \overline{h_1})$, of the system are traced along the varying parameter T_r. To represent $(T_r, T_r, 0)$, T_r is drawn as a straight line. For $(\overline{T_1}, \overline{T_2}, \overline{h_1})$, both $\overline{T_1}$ (middle curve) and $\overline{T_2}$ (lower curve) are shown. The stable solution is marked as a solid line, whereas a dashed line indicates the unstable solution. The symbol BP indicates a branch point where the two equilibrium points coincide. The equilibrium point at which Hopf (period doubling) bifurcation occurs is indicated by the symbol "*H* (PD)."

(Timmermann et al. 1999). A qualitatively new dynamical behavior emerges with $T_r = 30.5$°C. Strong amplitude modulations of ENSO with an 8.7-year-period modulating window that are associated with a bursting of extreme El Niño events occurring on a decadal-to-interdecadal time scale can be observed in Fig. 2c. The ENSO modulation in this regime seems to be very similar to that found by Timmermann et al. (2003) (see, Fig. 1c of Timmermann et al. 2003). In their study, the increasing strength of intrinsic nonlinearity controlled the stability of the oscillation and regime behavior. However, the decadal modulation and bursting mechanism of ENSO in our study is controlled not only by the oscillation itself, but it is also influenced by the increasing instability associated with T_r. A detailed analysis based on bifurcation analysis is presented in the next section.

4. Bifurcation analysis

To examine the characteristics of equilibrium solutions as well as the periodic orbits as T_r varies, we used MATLAB software and its mathematical continuation library MATCONT (Dhooge et al. 2006) to trace the fixed points and periodic solutions. During the trace, MATCONT finds the stability of the solution and detects singular points, such as a branch point (BP) or Hopf point, at which oscillatory solutions are birthed. Figure 3 displays the bifurcation diagram with respect to T_r. The equilibrium points are depicted as a function of increasing parameter values of T_r. In the figure, the diagram starts from the branch point at $T_r = 23$°C. When T_r is less than 23°C, there exist two equilibrium solutions. One is a stable permanent El Niño representing the radiative–convective equilibrium state,

$$(\overline{T_1}, \overline{T_2}, \overline{h_1}) = (T_r, T_r, 0),$$

with a flat thermocline ($\overline{h_1} = \overline{h_2} = 0$). The other is an unstable equilibrium (not shown). At $T_r = 23$°C, a branch point is detected and MATCONT reveals that the two branches exchange stabilities, yielding transcritical bifurcation. With this exchange of stability, the stable radiative–convective equilibrium state becomes an unstable saddle node. A saddle node is an equilibrium point that has one positive eigenvalue and two negative eigenvalues. Through the instability of the saddle node, the radiative–convective equilibrium strongly influences the ENSO life cycle. This is clearly illustrated in Fig. 4a. The trajectories starting from initial conditions initially scattered on the unit sphere of the saddle radiative–convective equilibrium state (open circle, hereafter saddle RC) converge toward the saddle RC through the direction corresponding to the negative eigenvalues and are repelled following the direction of the positive eigenvalue. The repelled trajectory, again, converges to another stable fixed point (closed circle). This stable fixed point represents the tropical climate state with a moderate zonal SST gradient maintained by the zonal wind stress of an easterly wind. The SST gradient measured by $\overline{T_1} - \overline{T_2}$ becomes continuously larger as T_r increases (Fig. 3). At the western Pacific box, the increasing heat flux that is proportional to the difference between T_r and $\overline{T_1}$ balances the moderately increasing zonal advection. At the eastern Pacific box, the heat flux increases more rapidly as T_r increases and balances the rapidly increasing vertical advection. Note that, above $T_r = 25$°C, $\overline{T_2}$ starts to decrease and the SST gradient becomes larger rapidly. Eventually, the SST gradient cannot be maintained by steady wind stress and becomes unstable through the Hopf bifurcation (*H* in Fig. 3). A simply closed curve in the phase space can be regarded as a limit cycle. It begins as T_r reaches 25.7°C (Fig. 4b). Hereafter, it is called the ENSO limit cycle. The equilibrium state represented by $(\overline{T_1}, \overline{T_2}, \overline{h_1})$, where the limit cycle originates, is characterized by a zonal SST gradient that gradually increases as T_r increases. The thermocline also declines more because it depends linearly on the zonal SST gradient. We denote this equilibrium state as the cold-tongue (CT) equilibrium (closed circle, here after, CT equilibrium). The dynamical structure at this equilibrium state is referred to as the "saddle foci." The basic mechanism of

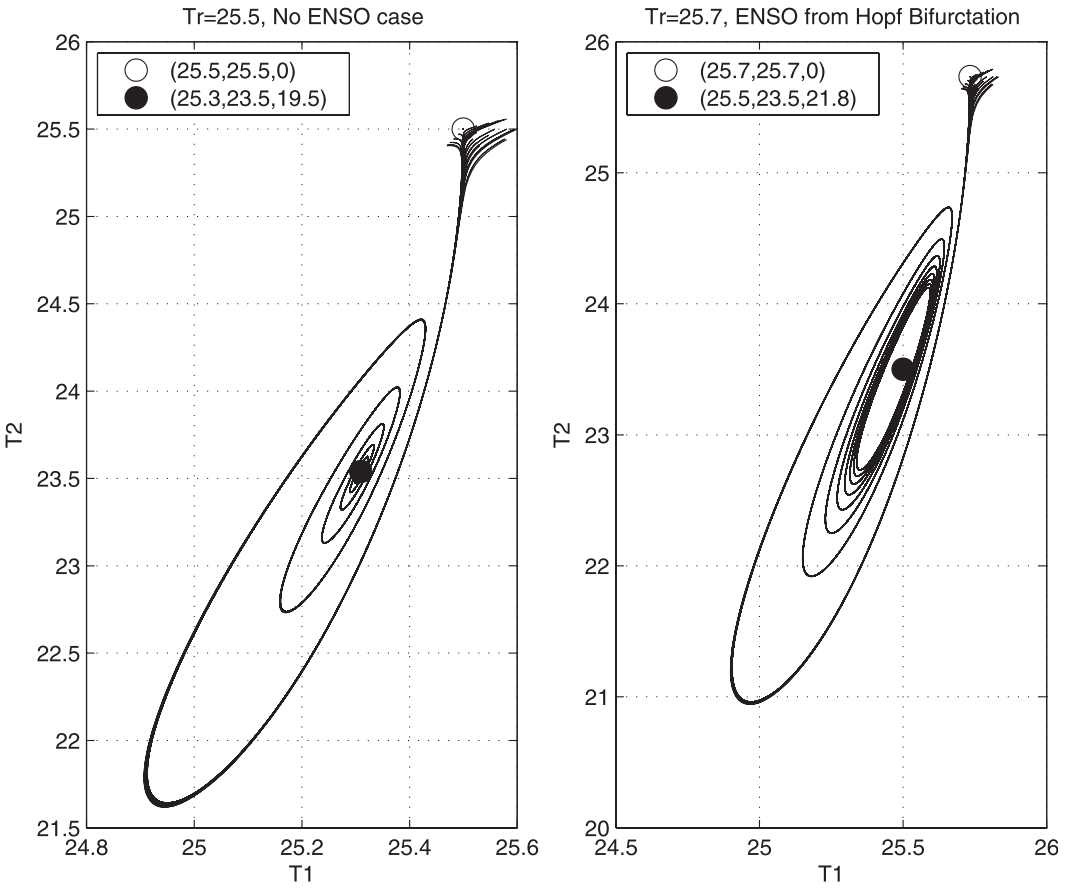

FIG. 4. Phase–space portrait of trajectories starting from 50 points uniformly distributed over the spherical surface centered at the saddle RC (open circle). The other equilibrium point (closed circle) found by MATCONT (Fig. 3) is also shown for (a) $T_r = 25.5$°C and (b) $T_r = 25.7$°C.

ENSO's limit cycle is clearly described by Jin (1996). The oscillation depicted in Fig. 4b exhibits an elongated structure toward the saddle RC owing to the characteristic feature of the saddle RC that attracts the orbit in one direction and repels in other directions. Linear stability analysis about the saddle RC indicates that after BP, there exist three eigenvalues: one positive and two negative. As T_r increases, the positive eigenvalue, starting from zero at BP, increases linearly with respect to T_r. The rate of increase is about 0.3 yr^{-1}, which is comparable to the intrinsic frequency of ENSO (not shown). The two negative eigenvalues remain constant. Therefore, the ENSO trajectory in the El Niño phase is attracted to the saddle RC and is repelled from the point and, therefore, exhibits an elongated structure along the axis connecting the saddle RC and the CT equilibrium. The modulation of ENSO by the saddle RC is clearly seen in Fig. 5, which shows the envelope of the ENSO oscillation after Hopf bifurcation. The amplitude of El Niño increases with T_r and the lower envelope, indicating that the amplitude of La Niña remains fairly constant.

A completely different ENSO behavior emerges at the period-doubling (PD) bifurcation as T_r reaches 29.8°C (Fig. 3). In this regime, ENSO exhibits multiple frequencies centered at the CT equilibrium. As in Fig. 2c, ENSO is characterized by intermittent bursting and relatively small oscillations. El Niño is stronger and La Niña is weaker in the bursting case (Fig. 2c); this asymmetry coincides with the observed trend of stronger El Niños and weaker La Niñas from the mid-1970s.

Timmermann et al. (2003) presented a parameter regime diagram in the ε–ζ plane, in their Fig. 6, with a fixed parameter value of $T_r = 29.5$°C. In this case, the system belongs to the single-oscillation (SO) regime at $\varepsilon = 1$, $\zeta = 0.13$, that is, the values used in our study. However, the point is very close to the PD boundary, which makes it very sensitive to small perturbation of any of the other parameters. Therefore, it would be helpful to construct a regime diagram to verify that the PD bifurcation due to an increase in T_r is not sensitive to ε and ζ values. Figure 6 (Fig. 7) shows the regime diagram in the T_r–ε (T_r–ζ) plane. In both figures, the amplitude-modulating regime (AMO)

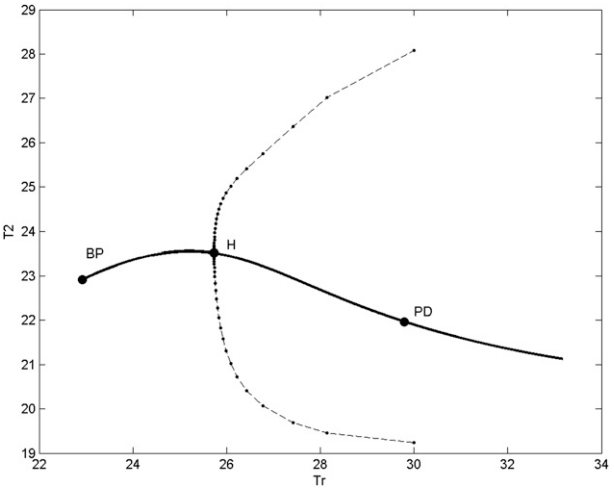

FIG. 5. Bifurcation diagram of T_2 as a function of T_r focusing on the oscillating regime. The solid line indicates stable fixed points, and the dashed line denotes unstable fixed points inside the existing limit cycle. Maximum and minimum values that the oscillation can attain for each T_r are indicated with dots.

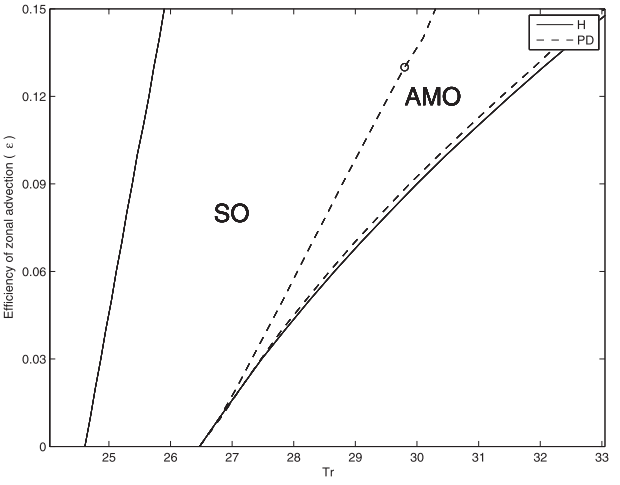

FIG. 6. Regime diagram in the T_r–ε plane. In the diagram, the boundary line of Hopf (period doubling) bifurcation is drawn with a solid (dashed) line. The symbol SO indicates the oscillation regime with a single frequency. The symbol "AMO" indicates a regime with amplitude-modulated oscillations. The open circle indicates the (T_r, ε) pair at which PD bifurcation occurs in this study.

occupies a large area for a realistic range of the parameters. This implies that the PD bifurcation due to an increase in T_r is robust and does not critically depend on the specific value of ε or ζ in a quite large area of the regime diagram. By calculating $dT_r/d\varepsilon$ of the PD curve passing through $T_r = 29.8$°C in Fig. 6, we are able to estimate how sensitive the PD bifurcation is to T_r as ε increases. $dT_r/d\varepsilon$, the sensitivity, is 27.8°C per unit variation of ε. Therefore, the increase of the nonlinear feedback strength for zonal advective feedback delays the PD bifurcation. The same analysis can be conducted with the parameter ζ and $dT_r/d\zeta$, which in this case is -4.5°C per unit variation of ζ (Fig. 7). Therefore, the increase of the nonlinear feedback strength for the thermocline feedback, on the other hand, advances the PD bifurcation. However, the sensitivity is approximately 6-times less effective in changing the timing of the PD bifurcation.

Figure 8 shows the ENSO limit cycle for selected T_r values in T_1–T_2 phase plane. As revealed in the bifurcation analysis (Fig. 3), the two curves (green, blue) with T_r below 29.8°C exhibit oscillations with a well-defined single frequency. In the phase plane representation, the elongated feature of the ENSO life cycle along the saddle RC (square dot) is well depicted. The two curves (green, red) with T_r above 29.8°C exhibit oscillations with multiple frequencies. As T_r approaches 30°C, just after PD, one subcycle emerges within the preexisting outercycle. As T_r increases, oscillations with different amplitudes are successively generated. These successfully generated oscillations with different amplitudes can be interpreted as decadal ENSO modulations. Three oscillations constituting decadal modulations of ENSO are present when T_r is over 31°C. Because the instability of the saddle RC increases linearly with T_r, regardless of ENSO bifurcation, the outercycle after PD has a shape elongated in the direction of the saddle RC (square dot) in proportion to the value of T_r.

5. Transient run

Although bifurcation analysis revealed possible ENSO behavior according to T_r, this is steady behavior in the sense that T_r is fixed for each ENSO solution. In addition to this, ENSO in the real world is exposed to a continuously

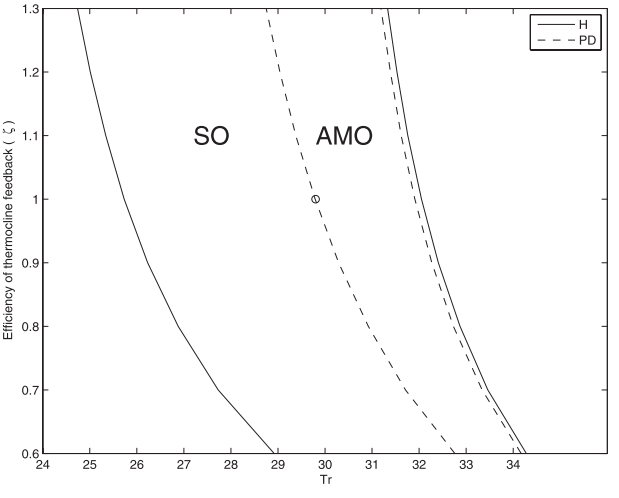

FIG. 7. As in Fig. 6, but shown in the T_r–ζ plane.

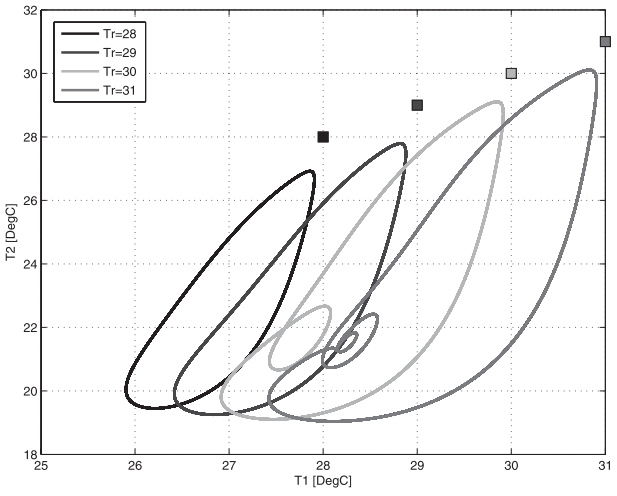

FIG. 8. Representation of the ENSO limit cycle in the T_1–T_2 plane with varying T_r. Each limit cycle and the corresponding T_r in the T_1–T_2 plane (square dot) are drawn with different colors, as indicated in the legend.

changing tropical mean state. In this section, ENSO behavior in a changing climate is examined by imposing the observed increasing trend of T_r on the model. The thermocline structure is also expected to change with the increase in T_r. However, it is difficult to estimate how the structure changes are associated with the increase in T_r. Although detailed examination is beyond the scope of this study, we test the influence of changes in the mean thermocline structure by varying H and T_c in addition to T_r. Here, H and T_c represent key factors of the gross mean thermocline structure, namely, mean thermocline depth and stratification of the thermocline, respectively. Based on the trend analysis shown in Fig. 1, T_r is formulated as

$$T_r = 29.5 + \lambda(t - 1900), \tag{5}$$

where $\lambda = 0.5$°C/100 yr is assumed to be the time-dependent forcing. Using Eq. (5), the transient run starts at $t = 1800$ yr, with an arbitrary chosen initial condition to remove features from initial transiencies and truncate the first 100 yr. Therefore, data from after 1900 is analyzed, which corresponds to a T_r of 29.5°C from the trend analysis.

Figure 9a shows the model behavior after $t = 1900$ yr. One striking difference from the steady response of a given T_r case is the delayed timing of the period-doubling bifurcation point. This point shifts toward a warmer climate and occurs at about year 2050, corresponding to $T_r = 30.25$°C. In the steady case, it occurs at $T_r = 29.8$°C (Fig. 3). This delayed response has been reported in a canonically similar dynamical system (Timmermann and Jin 2007). In Fig. 9a, the zonal SST gradient increases with time as the trend lines of T_1 and T_2 diverge. DiNezio et al. (2009) suggested that the zonal SST gradient, as a response to increased greenhouse gases, can be largely determined by the superposition of the ocean response to both a weakening of the Walker circulation and an increase in thermal stratification. With the configuration in Fig. 9a, the thermal stratification is influenced only by the surface changes because the subsurface temperature is fixed as $T_c = 16.0$°C. Therefore, the stratification effect is underestimated in this case and the increase in the zonal SST gradient, that is, a La Niña–like mean state, is achieved mainly through Bjerknes feedback. Because of the simplification of this model, the upwelling is directly coupled with the zonal SST gradient. Thus, the simulated La Niña–like mean state simply implies an enhancement of the Walker circulation in this model regardless of the thermal stratification change. DiNezio et al. (2009) showed that the ocean can be in a La Niña–like state even though the atmosphere slows down the Walker circulation. Unfortunately, this model cannot test this possibility.

In Fig. 9b, we show the results obtained after adding the shoaling effect of mean thermocline depth in the transient run. Several studies have reported that the thermocline depth shoals and also significantly modulates ENSO behavior in the Intergovernmental Panel on Climate Change (IPCC) future scenarios (An et al. 2008; Yeh et al. 2006). To determine the impact of shoaling, parameter H in the T_{sub} formulation was decreased as T_r increased. It should also be noted that the change in the thermocline influences other parameters such as b, a measure of the efficiency of wind stress used to derive the west–east thermocline, although we do not consider this change in this study.

To find a reasonable estimate of H in each state of T_r, we first related T_r to the ocean subsurface temperature profile averaged over the eastern box using regression analysis. We used Simple Ocean Data Assimilation (SODA 2.0.2–4; Carton and Giese 2008) reanalysis from 1958 to 2006 and SST_{max} obtained by HadISST for practical estimation of T_r. Both SST_{max} and ocean subsurface temperatures are 40-month averages. Actual regression analysis was conducted by predicting the ocean subsurface temperature at each level averaged over the eastern box region. The regression analysis indicates that mean thermocline depth becomes shallower as T_r increases and the vertical temperature gradient along the thermocline becomes larger (Fig. 10). We define the central position of the steep gradient region as the mean thermocline depth. The mean thermocline depth at $T_r = 29.5$°C is about 100 m and becomes about 90 m at $T_r = 30.5$°C. Therefore, the shoaling trend is 10 m $(200\ \text{yr})^{-1}$. With this consideration, we simply parameterize H with

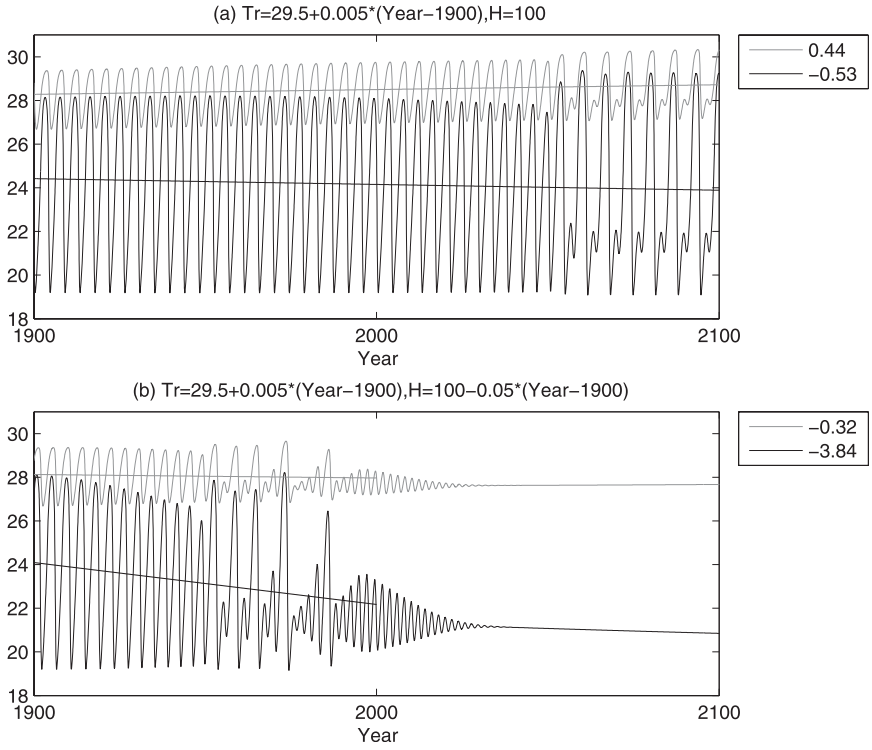

FIG. 9. Integration results for the low-order ENSO model constrained by time-varying external parameters: (a) $T_r = 29.5 + \lambda(t - 1900)$, (b) $H = 100 - 10\lambda(t - 1900)$. λ is 0.5°C (100 yr)$^{-1}$. T_1 (gray) and T_2 (black) are depicted, and trends are indicated using the same colors. Trends in (b) are calculated using data from the 100 yr from 1900 to 1999. Legends outside of the figure show the trends for T_1 and T_2 using the same color scheme. Trend values are shown for 200 yr, that is, the entire simulation period.

$$H = -10T_r + 395, \tag{6}$$

which yields 90 m in year 2100 corresponding to a T_r of 30.5°C. Although exact determination of the position of the mean thermocline depth is difficult, our goal is to achieve a qualitative understanding of the dependency of ENSO on mean thermocline change.

Figure 9b shows the behavior of the transient model after $t = 1900$ yr. A comparison of Figs. 9a and 9b indicates that shoaling of the mean thermocline depth advances the timing of the period-doubling bifurcation. This dynamical effect is quite strong; the delayed response due to the transiency of the external parameter T_r appears to be cancelled by the shoaling effect. Overall, the period doubling occurs in about the 1960s, which corresponds to a T_r of around 29.7°C, similar to the steady case. Aside from the timing of the bifurcation, another interesting feature caused by shoaling of the mean thermocline depth is the reduction in ENSO amplitude before PD as H decreases. However, this reduction conflicts with the observations (An and Wang 2000). Furthermore, the zonal SST gradient of the trend becomes very strong owing to the rapid decrease of the amplitude of El Niño. Even in the western Pacific, the trend is negative [−0.32°C (200 yr)$^{-1}$] owing to the relative cooling caused by zonal wind advection. Although there is a change in the stratification, the parallel shift of the mean thermocline depth toward the surface caused by shoaling has the effect of bringing the cold water to the surface, which causes significant cooling by upwelling. After the PD bifurcation, the oscillation rapidly becomes chaotic and collapses to a steady state before 2050.

The impact of changing stratification is tested by imposing T_c, as indicated below:

$$T_c = 16.0 \pm 0.5\lambda(t - 1900). \tag{7}$$

The increase (decrease) of stratification is simulated in Fig. 11a (Fig. 11b) by choosing the negative (positive) sign in (7). In this experiment, we multiplied λ by 0.5 to consider the slow adjustment of the subsurface. Similar to the shoaling effect, the increase in stratification shown in Fig. 11a advances the timing of the PD bifurcation. The PD bifurcation occurs at about year 2000. The increase in thermal stratification also increases the west–east SST

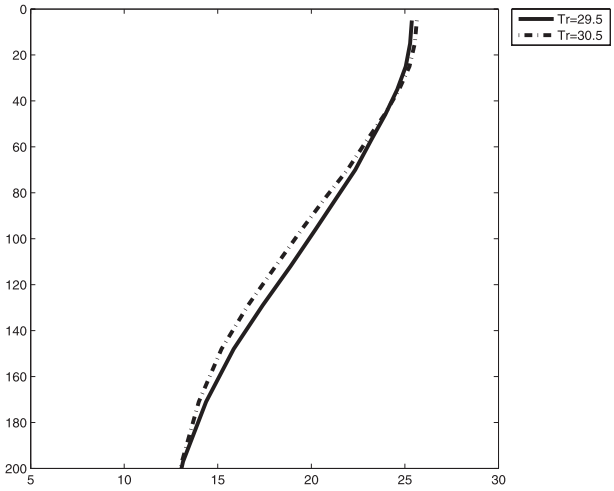

FIG. 10. Ocean subsurface temperature averaged over the eastern Pacific box (5°S–5°N, 155°–85°W) and regressed to T_r. Regression analysis was conducted for each level extending to 200 m. The solid line (dashed line) represents the vertical distribution of the ocean subsurface temperature at $T_r = 29.5$°C ($T_r = 30.5$°C).

gradient. This is due to the transport of relatively cold water with a given upwelling strength. Because of the strong coupling of upwelling with the SST distribution in this model, the upwelling strength also increases as the thermal stratification increases. Decreasing stratification does not result in PD bifurcation, as shown in Fig. 11b. Both T_1 and T_2 tend to increase. However, even with both positive trends, the zonal SST gradient became increasingly moderate—that is, a La Niña–like state.

6. Summary and discussion

This study proposes a possible explanation for the strong decadal amplitude modulation of ENSO observed after the mid-1970s during an observed warm period of the tropical ocean. The explanation is based on nonlinear dynamical systems theory, which permits multiregime behavior. The observed tropical warming in recent decades is characterized by a rapid increase in the warm-pool SST and a relatively weak increase in the eastern Pacific cold tongue SST (Fig. 1). Using a simple nonlinear ENSO model, Sun (2003) pointed out that an increase in the equatorial zonal SST gradient could lead to the amplification of ENSO. In this study, with a further increase in warming, we showed that the system enters into an amplitude modulation regime because of the intrinsic nonlinearity of the system. This phenomenon is controlled by the increasing instability of the saddle RC, that is, an equilibrium solution of the system representing a radiative–convective equilibrium state over the entire tropical ocean. The saddle RC interacts strongly with ENSO as tropical warming progresses. The interaction between the saddle RC and ENSO strongly constrains the amplitude of El Niño while the saddle RC has little influence on the amplitude of La Niña. Therefore, the interaction with the saddle RC brings El-Niño and La Niña asymmetry. At a certain stage of warming, severe destabilization of the saddle RC results in qualitatively new ENSO behavior that can be interpreted as an ENSO amplitude modulation regime. This modulation is consistent with the increase in ENSO irregularity observed in recent decades. In our model, ENSO after the bifurcation is characterized by multifrequency and bursting oscillations, which match well with the observed behavior of ENSO after the mid-1970s.

It should be noted that, in our interpretation, an increasing zonal SST gradient is an essential requirement for ENSO amplitude modulation. This is convincingly shown in section 5. DiNezio et al. (2009) showed that, in many models with future scenario runs, the mean zonal SST gradient in each model is determined as the superposition of the ocean response to a weakening of upwelling, which causes warming, accompanied by a weakening of Walker circulation and an increase in thermal stratification, which causes cooling. As discussed in section 5, the nonlinear ENSO model used in this study always goes into a La Niña–like mean state as T_r increases. However, this inevitably intensifies the Walker circulation, which in turn helps to sustain the La Niña–like mean state. This model, therefore, appears to have a bias toward a La Niña–like mean state.

Recently, Karnauskas et al. (2009) demonstrated that the equatorial Pacific zonal SST gradient strengthened from 1880 to 2005 during the boreal fall, when the gradient is normally strongest. To model the recent ENSO decadal modulation, an increased zonal SST gradient is, therefore, a crucial ingredient. Fundamental questions that remain to be answered are how future tropical Pacific warming will manifest and whether the zonal SST gradient will increase as it has over the last century. The latter depends on how the tropical ocean redistributes heat obtained by increased radiative fluxes from the ocean surface. The monitoring of vertical heat adjustment through the ocean is, therefore, essential. Future ENSO behavior will largely be determined by the answer to this question, as shown by the transient runs presented in section 5. Although the impact of the change in thermocline structure on ENSO was briefly considered in section 5, this study is far from a complete description of the full impact of vertical stratification of the ocean temperature on ENSO in a warming climate. The surface ocean, for instance, adjusts to temperature increases faster than the subsurface ocean (i.e., several decades behind) because of its slow dynamical adjustment, so that important factors

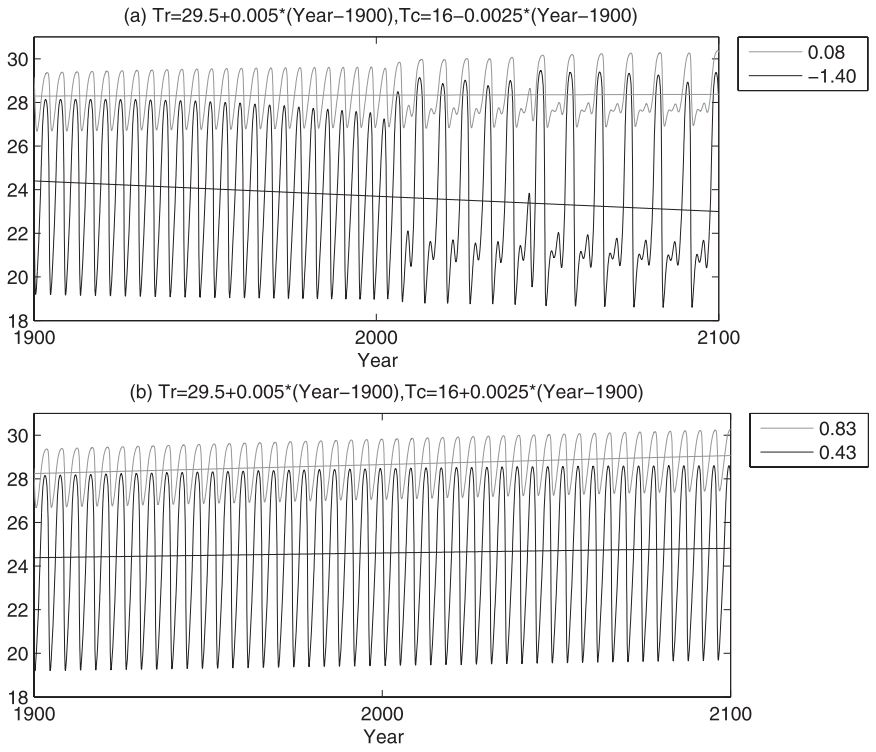

FIG. 11. As in Fig. 9, but external parameters were constrained with (a) $T_r = 29.5 + \lambda(t - 1900)$, $T_c = 16 - 0.5\lambda(t - 1900)$, and (b) $T_r = 29.5 + \lambda(t - 1900)$, $T_c = 16 + 0.5\lambda(t - 1900)$. λ is 0.5°C (100 yr)$^{-1}$.

controlling ENSO behavior, such as the sharpness of the thermocline, may continue to exert a large influence on ENSO as global warming evolves. One can imagine, for example, that the thermocline sharpens initially in response to global warming because of conspicuous surface warming with much less warming of the subsurface, which could lead to an increase in ENSO activity as well as a strong oceanic thermostat. However, after greenhouse gas concentrations have stabilized, that is, in the equilibrium state, we do not expect a sharp thermocline and increased ENSO activity (An et al. 2008). Figure 11b gives some insight into this possible scenario. With decreasing stratification in some phase of global warming, ENSO may return back to a simple and regular oscillating regime. In conclusion, both shoaling and increasing stratification cause ENSO to exhibit amplitude modulation. Furthermore, the timing of the PD bifurcation advances with these two effects as global warming progresses.

Although the simple nonlinear ENSO model is useful and reproduces many salient features of ENSO in a changing climate, there are some obvious caveats. First of all, the model simulates El Niño anomalies on the order of about 8°C, which is much larger than those observed. This is largely due to the too cold mean temperature of the eastern Pacific box. In Fig. 3, the equilibrium state of T_2 is too cold (below about 22°C), as compared to the observed mean eastern Pacific SST. More importantly, the zonal SST gradient, that is, T_1–T_2, is much stronger than the current climate condition, which is a source of instability for a bigger El Niño as discussed in section 4. La Niña also has temperatures that are too cold in the eastern box, and the equilibrium state is biased toward lower temperatures, as compared to the observed mean climate. Although we examined some dependencies of ENSO on the mean thermocline structure in section 5, these were only heuristic sensitivity tests for the T_{sub} parameterization and were far from complete. Furthermore, it should be noted that the subsurface temperature and thermocline structure used in this study were, at best, prescribed, although they do interact in nature. Based on these caveats, actual comparisons with the observed climate should be treated with caution, although the qualitative regime change revealed in this study is supported by the observations of a regime shift around the 1970s.

Acknowledgments. B.-M. Kim was supported by Korea Polar Research Institute (KOPRI) Project (PE10130) and Korea Meteorological Administration Research and Development Program under Grant RACS_2010-3005 (PN10060). S.-I. An was supported by the National

Research Foundation of Korea Grant funded by the Korean Government (NRF-2009-C1AAA001-2009-0093042).

APPENDIX

Derivation of T_{sub} Parameterization

Considering the structure of the mean ocean temperature profile, it is reasonable to use a tangent hyperbolic function for analytic representation in this simple model study. Then, the general form of the approximation for the mean ocean temperature profile $\overline{T}(z)$ can be written as

$$\overline{T}(z) = A + B\tanh\left[\frac{\overline{h} - z}{h^*}\right], \tag{A1}$$

where $\overline{h}$ is the mean thermocline depth, A is the temperature at the mean thermocline depth, B is the half-width of the steep gradient region of the mean thermocline, and h^* is a parameter representing the steepness of the mean thermocline. Following previous studies, T_{sub} is the temperature just below the mixed layer that depends strongly on the depth of the thermocline. As a simple representation, it is assumed that the thermocline depth anomaly causes vertical displacement of the mean ocean temperature profile. Therefore, the ocean temperature profile with the thermocline depth anomaly (h') can be represented as

$$\overline{T}(z; h') = A + B\tanh\left[\frac{\overline{h} + h' - z}{h^*}\right], \tag{A2}$$

where the positive anomaly of h' shifts the profile downward.

In Eq. (A2), $\overline{h}$ can be decomposed into a zonal mean component H and the deviation from the zonal mean at the eastern box $\overline{h}_2$. Here, h_1 and h_2 are thermocline anomalies from the zonal mean thermocline depth. Actually, H is a reference thermocline depth that can be chosen arbitrarily. However, Eq. (3) guarantees that $h_1 + h_2$ equals zero at the equilibrium state, which makes it physically reasonable to assign H as a basinwide or zonally averaged mean thermocline depth. Here, $\overline{h}_2$ can be obtained by time averaging h_2 after initial transiency. This is because $\overline{h}_1 + \overline{h}_2 \cong 0$ despite the difference between the time mean state and the equilibrium state. Replacing $\overline{h}$ with $H + \overline{h}_2$, and using $h_2 = \overline{h}_2 + h'$, Eq. (A2) can be expressed in terms of h_2, an anomaly from the zonal mean thermocline depth:

$$\overline{T}(z; h_2) = A + B\tanh\left[\frac{H + h_2 - z}{h^*}\right]. \tag{A3}$$

Assuming $A = (T_r + T_c)/2$, $B = (T_r - T_c)/2$, we get

$$\overline{T}(z; h_2) = (T_r + T_c)/2 + (T_r - T_c)/2\tanh\left[\frac{H + h_2 - z}{h^*}\right]. \tag{A4}$$

Now, T_{sub} in Eq. (4) can be obtained by defining it as simply $\overline{T}(z_0; h_2)$. Here, z_0 is the depth where the characteristic upwelling occurs. This completes the derivation.

REFERENCES

An, S. I., and B. Wang, 2000: Interdecadal change of the structure of the ENSO mode and its impact on the ENSO frequency. *J. Climate,* **13,** 2044–2055.

——, and F.-F. Jin, 2001: Collective role of thermocline and zonal advective feedbacks in the ENSO mode. *J. Climate,* **14,** 3421–3432.

——, J.-S. Kug, Y.-G. Ham, and I.-S. Kang, 2008: Successive modulation of ENSO to the future greenhouse warming. *J. Climate,* **21,** 3–21.

Cane, M., A. C. Clement, A. Kaplan, Y. Kushnir, D. Pozdnyakov, R. Seager, S. E. Zebiak, and R. Murtugudde, 1997: Twentieth-century sea surface temperature trends. *Science,* **275,** 957–960.

Carton, J. A., and B. S. Giese, 2008: A reanalysis of ocean climate using Simple Ocean Data Assimilation (SODA). *Mon. Wea. Rev.,* **136,** 2999–3017.

Clement, A. C., R. Seager, M. A. Cane, and S. E. Zebiak, 1996: An ocean dynamical thermostat. *J. Climate,* **9,** 2190–2196.

Collins, M., 2005: El Niño- or La Niña-like climate change? *Climate Dyn.,* **24,** 89–104.

Cubasch, U., and Coauthors, 2001: Projections of future climate change. *Climate Change 2001: The Scientific Basis,* J. T. Houghton et al., Eds., Cambridge University Press, 527–582.

Dhooge, A., W. Govaerts, and Y. A. Kuznetsov, 2003: MATCONT: A MATLAB package for numerical bifurcation analysis of ODEs. *ACM Trans. Math. Software,* **29,** 141–164, doi:10.1145/779359.779362.

DiNezio, P. N., A. Clement, G. A. Vecchi, B. J. Soden, B. P. Kirtman, and S. K. Lee, 2009: Climate response of the equatorial Pacific to global warming. *J. Climate,* **22,** 4873–4892.

Fedorov, A. V., and S. G. Philander, 2000: Is El Niño changing? *Science,* **288,** 1997–2001.

Guilyardi, E., 2006: El Niño mean state seasonal cycle interactions in a multi-model ensemble. *Climate Dyn.,* **26,** 329–348.

Jin, F.-F., 1996: Tropical ocean interaction, Pacific cold tongue, and El Niño Southern Oscillation. *Science,* **274,** 76–78.

Karnauskas, K. B., R. Seager, A. Kaplan, Y. Kushnir, and M. A. Cane, 2009: Observed strengthening of the zonal sea surface temperature gradient across the equatorial Pacific Ocean. *J. Climate,* **22,** 4316–4321.

Knutson, T. R., and S. Manabe, 1995: Time-mean response over the tropical Pacific due to increased CO_2 in a coupled ocean–atmosphere model. *J. Climate,* **8,** 2181–2199.

Kug, J.-S., K. P. Sooraj, F.-F. Jin, Y.-G. Ham, and D.-H. Kim, 2010: A possible mechanism for El Niño like warming in response to the future greenhouse warming. *Int. J. Climatol.,* in press, doi:10.1002/joc.2163.

Latif, M., and N. S. Keenlyside, 2008: El Nino–Southern Oscillation response to global warming. *Proc. Natl. Acad. Sci. USA,* **106,** 20 578–20 583.

Lau, N. C., S. G. H. Philander, and M. J. Nath, 1992: Simulation of ENSO-like phenomena with a low-resolution coupled GCM of the global ocean and atmosphere. *J. Climate,* **5,** 284–307.

Meehl, and Coauthors, 2007: Global climate projections. *Climate Change 2007: The Physical Science Basis,* S. Solomon et al., Eds., Cambridge University Press, 747–845.

Merryfield, W. J., 2006: Changes to ENSO under CO_2 doubling in a multimodel ensemble. *J. Climate,* **19,** 4009–4027.

Rayner, N. A., D. E. Parker, E. B. Horton, C. K. Folland, L. V. Alexander, and D. P. Rodwell, 2003: Global analyses of sea surface temperature, sea ice, and night marine air temperature since the late nineteenth century. *J. Geophys. Res.,* **108,** 4407, doi:10.1029/2002JD002670.

Sun, D.-Z., 1997: El Niño: A coupled response to radiative heating? *Geophys. Res. Lett.,* **24,** 2031–2034.

——, 2003: A possible effect of an increase in the warm-pool SST on the magnitude of El Niño warming. *J. Climate,* **16,** 185–205.

Timmermann, A., and F.-F. Jin, 2007: ENSO instability revisited. *Extreme Events: Proc. 15th Aha Huliko'a Hawaiian Winter Workshop,* Honolulu, HI, U.S. Office of Naval Research, School of Ocean and Earth Science and Technology, and Department of Oceanography, University of Hawaii at Manoa, 125–130.

——, J. Oberhuber, A. Bacher, M. Esch, M. Latif, and E. Roeckner, 1999: Increased El Niño frequency in a climate model forced by future greenhouse warming. *Nature,* **398,** 694–696.

——, F.-F. Jin, and J. Abshagen, 2003: A nonlinear theory for El Niño bursting. *J. Atmos. Sci.,* **60,** 152–165.

Vecchi, G., and B. Soden, 2007: Global warming and the weakening of the tropical circulation. *J. Climate,* **20,** 4316–4340.

——, A. Clement, and B. J. Soden, 2008: Examining the tropical Pacific's response to global warming. *Eos, Trans. Amer. Geophys. Union,* **89,** doi:10.1029/2008EO090002.

Wang, B., and S.-I. An, 2001: Why the properties of El Niño changed during the late 1970s. *Geophys. Res. Lett.,* **28,** 3421–3432.

Yeh, S.-W., Y.-G. Park, and B. P. Kirtman, 2006: ENSO amplitude changes in climate change commitment to atmospheric CO_2 doubling. *Geophys. Res. Lett.,* **33,** L13711, doi:10.1029/2005GL025653.

Zebiak, S. E., and M. A. Cane, 1987: A model El Niño–Southern Oscillation. *Mon. Wea. Rev.,* **115,** 2262–2278.